AIChE

Sherwood Number in Flow Through Parallel Porous Plates (Microchannel) due to Pressure and Electroosmotic Flow

Nallapusa Vennela, Sourav Mondal, and Sirshendu De
Dept. of Chemical Engineering, Indian Institute of Technology, Kharagpur, Kharagpur 721302, India

Subir Bhattacharjee
Dept. of Mechanical Engineering, University of Alberta, Edmonton, AB, Canada T6G 2G8

DOI 10.1002/aic.12713
Published online August 4, 2011 in Wiley Online Library (wileyonlinelibrary.com).

An expression for Sherwood number is developed from first principles for combined pressure-driven and electroosmotic flow in a porous rectangular microchannel. This quantifies the mass transfer of an electrically neutral solute in the microchannel and is useful for designing microfluidic devices and porous media flows. The convective-diffusive species balance equation, coupled with the velocity field, is solved within the mass transfer boundary layer utilizing similarity method. From the simulations, it is observed that the Sherwood number increases as the electric double layer near the channel wall becomes more compact (as manifested through a decrease in the Debye length), and it reaches a constant value around the scaled Debye length of 40. The Sherwood number becomes constant at higher Debye lengths as electrokinetic effects become negligible. A detailed analysis of dependence of Reynolds number, dimensionless permeation velocity, ratio of driving force and scaled Debye length on Sherwood number is presented. © 2011 American Institute of Chemical Engineers AIChE J, 58: 1693–1703, 2012
Keywords: porous media, mass transfer, Sherwood number, permeation, Debye length

Introduction

Transport of chemical species due to convection and diffusion is central to mass transfer operations in classical process engineering applications. Such mass transfer operations are generally analyzed by assuming the processing environments (the systems) to be macroscopic. This allows assumptions, such as, fully developed flow, quasi one-dimensional transport, and negligible surface interactions of channel walls, complete decoupling of transport of uncharged solute species from ion transport, and so forth. In many modern applications, the processing environments used are being miniaturized progressively. Applications of these systems include microelectronics, biomedical separations and diagnostics, and various "lab-on-chip" processes. Mass transfer analysis is of paramount importance for prediction of transport phenomena in microstructured media such as gels, biofilms, microbial flocs, and granular porous media.[1–3] Furthermore, module design of separation processes like membrane filtration, electro-deionization, ion exchange, etc., have attained a state of sophistication where the mass transfer occurs in submillimeter, and more likely, mircoscale and nanoscale flow channel geometries. In this context, it is perhaps pertinent to assess the suitability of classical mass transfer concepts in designing various microscale and nanoscale transport and separation processes.

An interesting aspect of microscale flows is the relative importance of the electrical charge of the channel walls on the fluid flow and mass transport. Electroosmotic effects are widely used to control the liquid flow and the associated transport processes in microscale devices.[4–9] Various applications of electrokinetic phenomena in porous media are reported. Some of these are, salt rejection through membrane pores in reverse osmosis or nanofiltration,[10–12] transdermal iontophoretic drug delivery (which is one of the most promising novel drug delivery system),[13,14] transport in hydrogels,[3,14] as well as alternating current (AC) electrokinetic and pulsed field electrokinetic separations.[15–19] AC electroosmosis in microchannels packed with a porous media is also reported.[20] A pertinent application of mass transfer driven by electroosmotic flow through a porous microchannel is observed in transdermal delivery of drugs.[13,14] This process involves controlled migration of drugs, such as insulin, into the skin or tissue under the influence of an electrical potential gradient.[13,21,22] The skin is negatively charged, acts as permselective membrane to cations. The solute-rejecting semipermeable wall provides preferential passage of electrolytes and desired smaller sized species.[23] In the process, bigger sized neutral molecules are rejected. The rejected solutes form a mass transfer boundary layer near the wall. This boundary layer dictates the mass transfer and finally permeation rate through the porous wall.

The present analysis can also be applied to predict the permeation of neutral solutes in microhollow fiber membrane bioreactor,[24] which is widely used for collection of analytes including drugs, metabolites, peptides, and proteins. This study inferentially discusses the diffusive mass transfer of neutral solutes and how it affects the recovery process. Understanding of diffusive mass transport is especially critical during *in vivo* recovery of larger peptides and proteins.[3]

Correspondence concerning this article should be addressed to S. De at sde@che.iitkgp.ernet.in.

Another application is membrane-based separation for emulsion where a dilute emulsion can be subjected to external electric field in microchannel. In this case, some of the suspended droplets are attracted towards the wall, allowing them to pass through the membrane. Such a process can be extremely useful in a variety of applications involving separation of the components of a microemulsion.[16]

An appropriate mass transfer analysis of the above processes in presence of electroosmotic flow enables efficient design of such systems. Many of these processes involve transport of a solute, which may not even be charged, and thus, are not subject to direct electrokinetic forcing in presence of an electric field. Yet, the electrokinetic flow of the ionic species (the electrolyte), and their polarization near the charged channel walls can influence the mass transfer of these uncharged solutes.[15] However, to the authors' knowledge, simple models of mass transfer analysis through charged porous microchannels in conjunction with electroosmotic flow are not available in literature.

Extensive studies on flow through microchannels have been reported addressing the fluid flow and heat transfer.[25–30] In case of heat transfer, Nusselt number for combined pressure and electroosmotically driven flows in microchannel and effects of viscous dissipation are reported.[31,32] However, in that study, a fully developed thermal boundary layer under constant wall heat flux condition is considered. In contrast, in case of mass transfer analysis, since mass transfer boundary layer grows slowly (due to higher Schmidt number). Therefore, the fully developed mass transfer boundary layer is not realistic in microchannel systems. Furthermore, if the channel wall is porous, the constant flux condition has to be replaced by a Robin mixed boundary condition. Therefore, mathematical analysis of mass transfer in microchannels and biological systems considering the role of the channel wall charge are relatively rare.[2,33] Liapis and Grimes[34] developed the expression of film mass transfer coefficient for purely electroosmotic flow in packed bed in impervious circular pores. They showed that for the same volumetric flow rate, the film mass transfer coefficient of electroosmotically driven flows is proportional to that for pressure-driven flows. However, their solution did not specify the values of the leading coefficients in the expression of mass transfer coefficient, relegating this to experimental measurements.

In this study, we present a detailed mass transport analysis of an electrically neutral solute dissolved or suspended in an electrolyte solution flowing through a permeable-wall electrified slit microchannel. The analysis is conducted by considering a combined pressure driven and electroosmotic flow in the porous microchannel. Analytical solution of average Sherwood number is developed from the first principles. Effects of various process parameters, namely, permeation velocity, electrolyte concentration, Reynolds number in the channel and ratio of pressure driven to electroosmotic flow on the Sherwood number are investigated. The developed relationship would be of immense help in efficient design and control of microscale flow and separation processes, and may substitute detailed numerical calculations of such processes.

Mathematical formulation

Figure 1 shows the two-dimensional electroosmotic flow in the porous microchannel of length L and height $2h$, containing a 1:1 symmetric electrolyte solution with constant

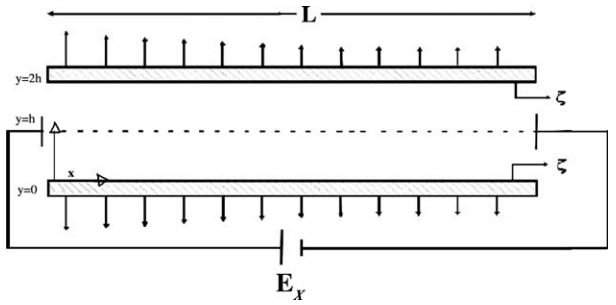

Figure 1. Flow geometry of a slit microchannel with a porous wall.

The channel half-height is *h*. The two walls are semipermeable, allowing the solvent and the electrolyte to pass through, but rejecting the uncharged solute completely.

dielectric constant, ε. The inner surfaces of the channel are charged at the wall potential, ζ. Upon imposition of a uniform external electric field of strength E_x, and a pressure grad*ie*nt ($p_x = \frac{dP}{dx}$), the fluid in the channel is set into motion due to the combined effect of Poiseuille and electroosmotic flow. It may be noted that the coordinate system is fixed at the lower surface of the channel.

Potential field

The governing equation, for electric double layer potential (for small surface potentials) is given below,[17]

$$\frac{d^2\psi}{dy^2} = \frac{2n_\infty Z^2 e^2 \psi}{\varepsilon k_B T} \tag{1}$$

The above equation can be written as,

$$\frac{d^2\psi}{dy^2} = \kappa^2 \psi$$

where, κ is inverse double layer thickness and is given by, $\kappa = \left(\frac{2n_\infty z^2 e^2}{\varepsilon k_B T}\right)^{\frac{1}{2}}$.

The above governing equation Eq. 1 is subjected to the following boundary conditions,

$$\text{at } y = 0, \quad \Psi = \zeta \tag{1a}$$

$$\text{at } y = h, \quad \frac{d\psi}{dy} = 0 \tag{1b}$$

Solution of Eq. 1 provides an expression of surface potential as,

$$\psi = \frac{\varsigma \cosh(\kappa y - \kappa h)}{\cosh(\kappa h)} \tag{2}$$

Velocity field

The governing equation, for fully developed, one-dimensional axial velocity field for the electrolyte solution can be expressed under Debye-Huckel approximation as,[17]

$$\frac{d^2 u_x}{dy^2} = -\frac{p_x}{\mu} - u_{HS}\,\kappa^2 \ \frac{\cosh(\kappa h - \kappa y)}{\cosh(\kappa h)} \tag{3}$$

where, u_x is the axial velocity, u is the fluid viscosity, and κ is the inverse of Debye length, and $u_{HS} = \frac{-\varepsilon E_x \zeta}{\mu}$. Following are the relevant boundary conditions,

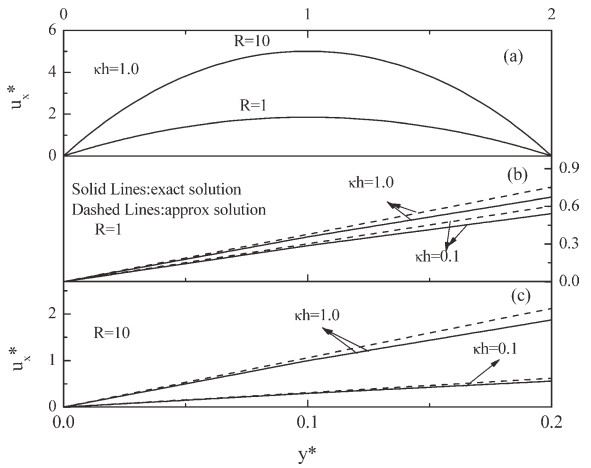

Figure 2. Velocity profiles in the channel.

(a) Complete velocity profile, Eq. 4a for $\kappa h = 1.0$ and $R = 1$ and 10; (b) Comparison of exact velocity profile (Eq. 4a) with approximated profile (Eq. 5) for κh =0.1 and 1.0 at $R = 1$; and (c) Comparison of exact velocity profile (Eq. 4a) with approximated profile (Eq. 5) for κh =0.1 and 1.0 at $R = 10$.

$$\text{at } y = 0, \quad u_x = 0 \tag{3a}$$

$$\text{at } y = 2h, \quad u_x = 0 \tag{3b}$$

Using the above boundary conditions, the expression for the axial velocity profile becomes,

$$u_x = \frac{p_x h^2}{\mu}\left(y^* - \frac{y^{*2}}{2}\right) + u_{Hs}\left[1 - \frac{\cosh\{\kappa h(1-y^*)\}}{\cosh(\kappa h)}\right] \tag{4}$$

where, $y^* = y/h$.

In the above expression, the term containing $p_x(\frac{dP}{dx})$ can be substituted by the cross section area averaged velocity due to poiseulle flow, as $u_p = \frac{p_x h^2}{3\mu}$. Thus, the velocity profile becomes,

$$u_x = 3u_p\left(y^* - \frac{y^{*2}}{2}\right) + u_{Hs}\left[1 - \frac{\cosh\{\kappa h(1-y^*)\}}{\cosh(\kappa h)}\right] \tag{4a}$$

It may be noted that our interest in velocity profile is the part that lies within mass transfer boundary layer. Typical values of solute diffusivity to be considered in such cases are in the order of 10^{-10} to 10^{-11} m^2/s, that leads to Schmidt number of the order of 10^4 to 10^5. As the thickness of mass transfer boundary layer is inversely proportional to Schmidt number, we can safely assume that in the micro-channel the mass transfer boundary layer lies within 10% of the half channel height. However, this assumption is verified in the subsequent sections.

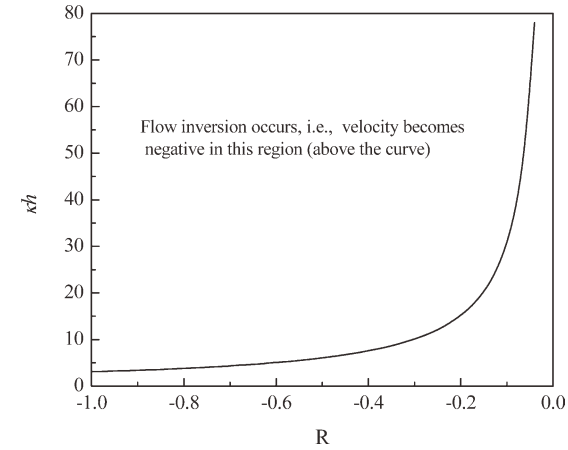

Figure 3. Feasible range of velocity for negative values of R varying with κh.

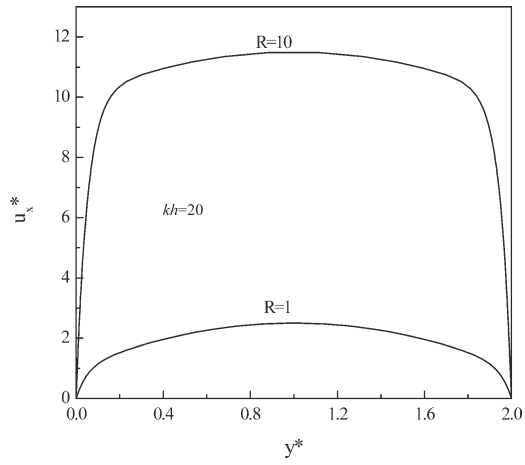

Figure 4. Actual velocity profile at κh =20 at R = 1 and 10.

***Velocity profile for small values of* κh:**

With the assumption stated earlier, in the mass transfer boundary layer, y^* in Eq. 4a is less than 0.1. In that limit, one can approximate $\sinh(\kappa h y^*)$ as $\kappa h y^*$ and $\cosh(\kappa h y^*)$ as 1. Similar type of approximation was used by Zhou et al.[30] Therefore, the approximated form of velocity profile in the mass transfer boundary layer is obtained from Eq. 4a as,

$$u_x^* = 3\left[1 + \frac{R}{3}\,\kappa h\,\tanh(\kappa h)\right]y^* \tag{5}$$

where, $R = \frac{u_{Hs}}{u_p}$ and $u_x^* = \frac{u_x}{u_p}$. The complete velocity profile is shown in Figure 2a, for $\kappa h = 1.0$ and R values at 1 and 10. The exact Eq. 4a and the approximate Eq. 5 velocity profiles are shown up to $y^* = 0.1$ in Figures 2b,c for $R = 1$ and $R = 10$, respectively. Figures 2b,c clearly show that velocity profiles are really linear till $y^* = 0.1$ and the approximate profile Eq. 5 matches closely with the exact profile up to $y^* = 0.1$, i.e., within 10% of channel half height. Equation 5 holds good when $\kappa h \leq 3$ within 5% deviation. When $\kappa h > 3$ approximated velocity profile (Eq. 5) deviates from exact velocity profile (Eq. 4a) more than 5%.

A feasible range of variables namely κh and negative R (electroosmotic flow opposing pressure-driven flow) for which the overall velocity field does not show inversion is presented ion Figure 3. This figure is produced by solving Eq. 4a. It is clear from this figure that inversion of velocity field can be avoided for all combinations of κh and R below the curve presented in the figure. For $\kappa h = 30$, the feasible value of R is greater than -0.1. As the value of R increases feasibility region increases. For low values of R, feasibility domain decreases, and the solution exists for smaller κh.

***Velocity profile at higher values of* κh:**

Complete velocity profile Eq. 4a is presented in Figure 4 at higher value of $\kappa h = (=20)$ for $R = 1$ and $R = 10$. It is clear from this figure that even for higher values of κh, the velocity profile is linear within 10% of channel half height

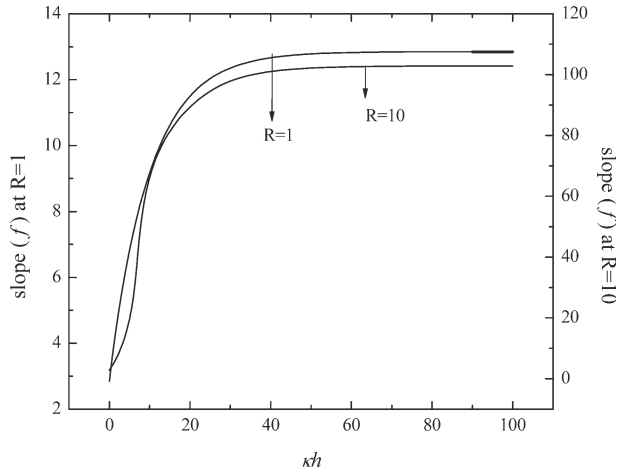

Figure 5. Slope of linear velocity profile versus κh for $R = 1$ and 10.

i.e., $y^* = 0.1$. Thus, it can be stated that velocity profile is linear till $y^* = 0.1$ from the wall for any value of κh. Similar observation is made by Liapis and Grimes [34]. Therefore, within 10% of the channel half height ($y^* = 0.1$), the velocity profile can be expressed as,

$$u_x^* = f\, y^* \tag{6}$$

where, f is the slope of velocity profile between $y^* = 0$ and 0.1. A close look at Eq. 5 reveals that f must have the following form,

$$f = 3 + R\ g(\kappa h) \tag{7}$$

In the above expression, first term of right-hand side is the slope of pure poiseulle flow and the second term corresponds to electroosmotic flow. g is a function of scaled value of inverse Debye length. Variation of f with κh for $R = 1$ and $R = 10$ is shown in Figure 5. Expression of g can be obtained by plotting f-3/R with κh. This is shown in Figure 6 for the values of $R = 1$ and 10. The variation is of the form of Langmuir function,

$$g = \frac{A\kappa h}{1 + B\kappa h} \tag{7a}$$

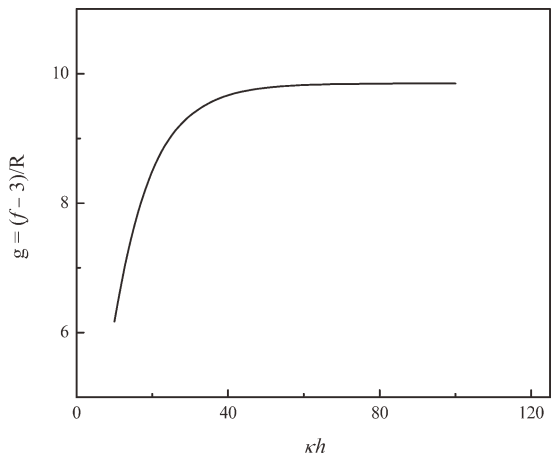

Figure 6. Variation of g with κh at $R = 1$ and $R = 10$.

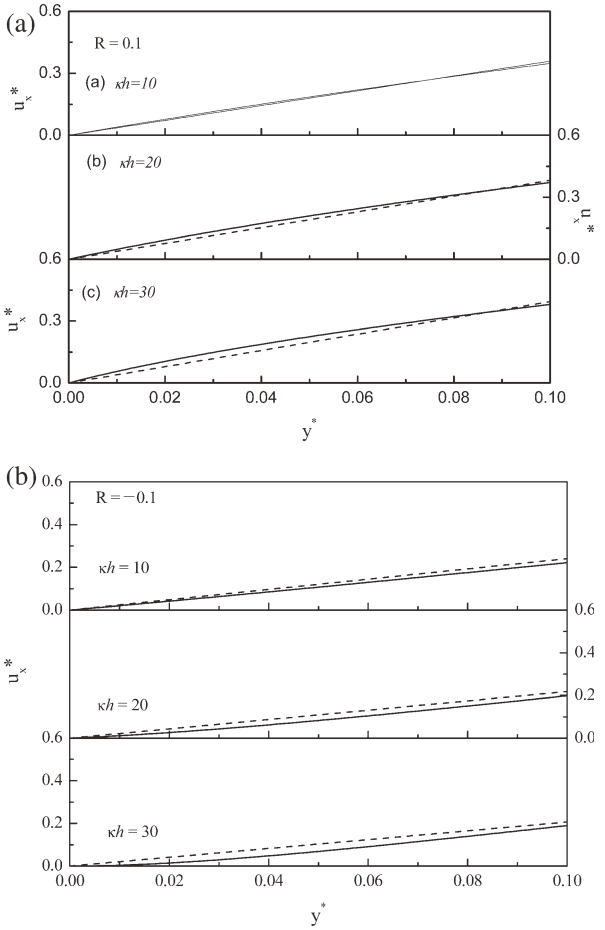

Figure 7. (a) Comparison of exact velocity profile (Eq. 4a) and the linear one (Eq. 10) at various values of κh and $R = 0.1$; (b) comparison of exact velocity profile (Eq. 4a) and the linear one (Eq. 10) at various values of κh and R = −0.1.

Solid lines: exact solution; Dashed lines: approximated solution

Equation 7a can be rewritten as,

$$\frac{1}{g} = \frac{1}{A\kappa h} + \frac{B}{A} \tag{7b}$$

As is shown in Figure 6, it can be observed that g is constant after $\kappa h = 40$ and below it, g is increasing with κh. Hence, the expression of g is obtained as,

$$g = \frac{1.08\kappa h}{1 + 0.08\kappa h} \quad \text{for } 3 < \kappa h \le 40 \tag{8}$$

$$= 10 \quad \text{for } \kappa h > 40 \tag{9}$$

***Velocity profile for all values of* κh:**

From above two sections, it is summarized that velocity profile is linear up to $y^* = 0.1$ for all values of κh and R and the profiles are presented below. For $0.1 < \kappa h \le 3$ velocity profile is expressed by Eq. 5.

$$\text{for} \quad 3 < \kappa h \le 40 \qquad u_x^* = 3\left[1 + \frac{R}{3}\left(\frac{1.08\kappa h}{1 + 0.08\kappa h}\right)\right] y^* \tag{10}$$

$$\text{for} \quad \kappa h > 40 \qquad u_x^* = 3\left(1 + 10\,\frac{R}{3}\right) y^* \tag{11}$$

All the above velocity expressions can now be expressed in the generalized form as, $u_x^* = 3my^*$, where expression for m differs for different range of κh. A plot of linear velocity profile Eq. 10 and exact one Eq. 4a is presented in Figure 7a for different values of κh and for $R = 0.1$ and the same comparison is shown in Figure 7b for $R = -0.1$. It is observed from Figure 7a that in case of $R = 0.1$, a maximum of 5.2%, 13 and 18% deviation occur for $\kappa h = 10$, 20, and 30, respectively, between exact and approximate velocity profile. It is observed from Figure 7b that in case of $R = -0.1$, a maximum of 7.8, 8.0, and 9.0% deviation occur for $\kappa h = 10$, 20, and 30, respectively, between exact and approximate velocity profile. This analysis clearly indicates the validity of linear approximation within the feasible region of κh and negative R as shown in Figure 3. It may be emphasized that the $R \to 0$ indicates a purely pressure-driven flow and $R^{-1} \to 0$ implies a purely electroosmotic flow.

Solute transport in the slit microchannel

The transport of an electrically neutral solute that is retained by a semipermeable wall of the slit-microchannel is modeled here. We assume complete retention of the solute by the semipermeable walls of the channel, and no electrical or colloidal interaction of the solute with the channel wall or the electrolyte. As there is no charge on the solute, it does not experience any direct electrokinetic effect. Also, the electric field gradients across the small solutes are negligible to give rise to any electric polarization forces on the solutes. For solutes of low diffusivity and high Schmidt number ($\mu/\rho D$), the thickness of the mass transfer boundary layer is extremely small and lies close to the wall. Under these conditions, the expression for the axial (x-component) electrolyte solution velocity can be expressed as

$$\frac{u_x}{u_p} = \frac{3y}{h} m(\kappa h, R) \tag{12}$$

where, m is defined in earlier. In terms of nondimensional variables, the velocity profile becomes,

$$u_x^* = \frac{u_x}{u_p} = A_0 \frac{y}{h} \tag{13}$$

where, $A_0 = 3m$. Under steady-state, the species balance equation within the mass transfer boundary layer is,

$$u_x \frac{\partial c}{\partial x} + v_y \frac{\partial c}{\partial y} = D \frac{\partial^2 c}{\partial y^2} \tag{14}$$

where, c is the concentration of the solute, v_y is the y-component velocity and D is the solute diffusivity. Assuming a thin mass transfer boundary layer, $v_y \approx -v_w\ (x)$, Eq. 14 becomes in nondimensional form

$$A_1 y^* \frac{\partial c^*}{\partial x^*} - \frac{Pe_w}{4} \frac{\partial c^*}{\partial y^*} = \frac{\partial^2 c^*}{\partial y^{*2}} \tag{15}$$

where, the dimensionless quantities are:

$$x^* = \tfrac{x}{L}; y^* = \tfrac{y}{h}; c^* = \tfrac{c}{c_0}$$

$$A_1 = \tfrac{3}{16}\left(\mathrm{Re}Sc\tfrac{d_e}{L}\right) m(\kappa h, R); \mathrm{Re} = \tfrac{\rho u_p d_e}{\mu}; Sc = \tfrac{\mu}{\rho D}; Pe_w = \tfrac{v_w d_e}{D}$$

Here,

$$d_e = 4\frac{\text{wetted area}}{\text{wetted perimeter}} = 4\frac{w \times 2h}{2(w+2h)},$$

since w >> 2h we consider $w + 2h \approx w$, therefore $d_e = 4h$.

As shown in Figure 1, permeation velocity is a local velocity and it is a function of x. Permeation velocity (Pe_w in nondimensional form in Eq. 15) is allowed to vary along the length as a function of operating conditions.

Boundary conditions for Eq. 14 are,

$$\text{at } x = 0;\ c = c_0 \tag{16}$$

$$\text{at } y = 0;\ v_w c + D\frac{\partial c}{\partial y} = 0 \tag{17}$$

$$y \to \infty;\ c = c_0 \tag{18}$$

The above set of equations is solved for the lower surface of the microchannel; symmetric mass transfer boundary layer is formed on the upper surface of the channel as shown in Figure 1. Boundary layers from both the surfaces merge at the center of the channel at downstream locations from the entrance.

An order of magnitude analysis of Eq. 15 at the edge of the mass transfer boundary layer from the channel entrance leads to, $A_1\delta^* \frac{\Delta c^*}{x^*} \approx \frac{\Delta c^*}{\delta^{*2}}$. This gives the variation of the thickness of mass transfer boundary layer as $\delta^* = \left(\frac{x^*}{A_1}\right)^{1/3}$. It may be mentioned here that the presence of corner points in a rectangular channel changes the localization properties of the concentration field and can modify the scaling exponent. The present analysis does not consider this effect. Equation 15 admits a similarity solution with the similarity parameter, $\eta = \frac{y^*}{\delta^*} = A_1^{\frac{1}{3}} \frac{y^*}{x^{*1/3}}$. In terms of similarity parameter, Eq. 15 and its boundary conditions become,

$$\frac{d^2c^*}{d\eta^2} = \left(-\frac{\eta^2}{3} - B\right)\frac{dc^*}{d\eta} \tag{19}$$

$$at\ \eta = 0,\ Bc^* + \frac{dc^*}{d\eta} = 0 \tag{20}$$

$$at\ \eta \to \infty,\ c^* = 1 \tag{21}$$

where, $c^* = c/c_0; B = \frac{Pe_w x^{*1/3}}{4A_1^{1/3}}$. It may be noted here that the permeation flux through the porous wall (Pe_w) is inversely proportional to the thickness of the mass transfer boundary layer (δ^*). As discussed above, δ^* is proportional to $x^{*1/3}$. Thus, the quantity B, defined above is a constant. Solution of Eq. 19 with Eqs. 20 and 21 yields,

$$c^*(\eta) = K_1 \int_0^\eta \exp\left(-\frac{\eta^3}{9} - B\eta\right)d\eta + K_2 \tag{22}$$

$$K_1 = -\frac{B}{1 - BI} \tag{23}$$

$$K_2 = \frac{1}{1 - BI} \tag{24}$$

$$I = \int_0^\infty \exp\left(-\frac{\eta^3}{9} - B\eta\right)d\eta \tag{25}$$

The mass transfer coefficient is defined as,

$$k(c_w - c_0) = -D\left(\frac{\partial c}{\partial y}\right)_{y=0} \tag{26}$$

where, c_w is the solute concentration at the wall.

Making Eq. 26 nondimensional and expressing the derivative in terms of similarity parameter, we obtain,

$$Sh(x^*) = \frac{kd_e}{D} = -4\left(\frac{A_1}{x^*}\right)^{1/3} \frac{\left(\frac{dc^*}{d\eta}\right)_{\eta=0}}{c_w^* - 1} \tag{27}$$

Table 1. Values of I (Eq. 25) For Various Operating Conditions

$ReSc d_e/L = 4000$; $R = 0.1$				$ReSc d_e/L = 4000$; $R = -0.1$				$ReSc d_e/L = 4000$; $R = 1$			
	Pe_w				Pe_w				Pe_w		
κh	100	500	1000	κh	100	500	1000	κh	100	500	1000
1	0.51	0.11	0.07	1	0.51	0.116	0.07	1	0.53	0.12	0.07
30	0.55	0.12	0.07	30	0.46	0.10	0.06	30	0.73	0.18	0.09
100	0.55	0.12	0.07	100	0.45	0.10	0.06	100	0.74	0.18	0.1
$ReSc d_e/L = 7000$; $R = 0.1$				$ReSc d_e/L = 7000$; $R = -0.1$				$ReSc d_e/L = 7000$; $R = 1$			
	Pe_w				Pe_w				Pe_w		
κh	100	500	1000	κh	100	500	1000	κh	100	500	1000
1	0.59	0.14	0.07	1	0.59	0.13	0.08	1	0.62	0.14	0.08
30	0.63	0.15	0.08	30	0.54	0.12	0.07	30	0.83	0.21	0.11
100	0.64	0.15	0.08	100	0.53	0.12	0.07	100	0.84	0.21	0.11
$ReSc d_e/L = 10000$; $R = 0.1$				$ReSc d_e/L = 10000$; $R = -0.1$				$ReSc d_e/L = 10000$; $R = 1$			
	Pe_w				Pe_w				Pe_w		
κh	100	500	1000	κh	100	500	1000	κh	100	500	1000
1	0.65	0.15	0.08	1	0.65	0.15	0.08	1	0.67	0.16	0.09
30	0.69	0.16	0.09	30	0.59	0.13	0.07	30	0.89	0.23	0.12
100	0.70	0.16	0.09	100	0.58	0.13	0.07	100	0.90	0.24	0.12

It may be identified that $c_w^* = K_2$ and $\left(\frac{dc^*}{d\eta}\right)_{n=0} = K_1$. Using Eqs. 23 and 24, the expression of Sherwood number becomes,

$$Sh(x^*) = 4\frac{A_1^{\frac{1}{3}}}{I}x^{*-\frac{1}{3}} \tag{28}$$

The length averaged Sherwood number becomes

$$\overline{Sh_L} = \int_0^1 Sh(x^*)dx^* = 6\frac{A_1^{1/3}}{I} = \frac{6\left(\frac{3}{16}\mathrm{Re}Sc\frac{d_e}{L}m(\kappa h,R)\right)^{1/3}}{I} \tag{29}$$

The length averaged permeation parameter (average wall Peclet number) is obtained from the definition of B,

$$\overline{Pe_w} = \int_0^1 Pe_w dx^* = 6BA_1^{1/3} \tag{30}$$

In terms of average permeation parameter, the constant B is expressed as,

$$B = \frac{\overline{Pe}_w}{6A_1^{1/3}} \tag{31}$$

Thus, the final expression of average Sherwood number becomes,

$$\overline{Sh_L} = \frac{3.43\left(\mathrm{Re}Sc\frac{d_e}{L}m(\kappa h,R)\right)^{1/3}}{I} = \frac{3.43\left(\mathrm{Re}Sc\frac{d_e}{L}m(\kappa h,R)\right)^{1/3}}{\int_0^\infty \exp\left(-\frac{\eta^3}{9} - \frac{0.29\overline{Pe_w}}{\left(\mathrm{Re}Sc\frac{d_e}{L}m(\kappa h,R)\right)^{1/3}}\eta\right)d\eta} \tag{32}$$

No permeation: $\overline{Pe}_w = 0$, and without electric field and purely pressure-driven flow, $R = 0$; the expression of average Sherwood number becomes,

$$\overline{Sh_L} = 1.85\left(\mathrm{Re}Sc\frac{d_e}{L}\right)^{\frac{1}{3}} \tag{33}$$

The above expression becomes identical with Leveque's solution by For various values of $\overline{Pe}_w = 0$, $ReSc d_e/L$, R, and κh, the values of the integral I are tabulated in Table 1.

Enhancement of Sherwood number due to electroosmotic flow with no permeation at the wall

Enhancement of Sherwood number with electroosmotic flow compared to purely pressure-driven flow can be simply demonstrated by considering no permeation case ($\overline{Pe}_w = 0$). In this case, the enhancement in Sherwood number can be defined by dividing no permeation combined flow case with no permeation purely pressure-driven flow. The expressions for enhancement for different ranges of κh will differ and they are presented below.

$$\text{For} \quad 1 < \kappa h \le 3 \qquad E = \left[1 + \frac{R}{3}\kappa h \tanh(\kappa h)\right]^{1/3} \tag{34}$$

$$\text{For} \quad 3 < \kappa h \le 40 \qquad E = \left[1 + \frac{R}{3}\left(\frac{1.08\kappa h}{1 + 0.08\kappa h}\right)\right]^{1/3} \tag{35}$$

$$\text{For} \quad \kappa h > 40 \qquad E = \left[1 + 10\frac{R}{3}\right]^{1/3} \tag{36}$$

The above given expressions are for electric filed assisting the flow. Validity of the analytical solution presented above is compared with the numerical solution. Numerical solution of Eq. 15 is carried out using one dimensional space-time discretization technique using PDEPE function of MATLAB 7.8.

Selection of operating parameters

To emulate flows in slit-channels of dimensions representing typical microchannels, following range of various parameters are selected: κh 0.1–100; the average velocity in the channel: 1 cm/s. For a channel equivalent diameter of 200 μm and kinematic viscosity (of water) 10^{-6} m^2/s, the Reynolds number ($\mathrm{Re} = \rho u_0 d_e/\mu$) becomes in the order of 2. Typical ratio of d_e/L for such microchannel varies between 0.02 to 0.1. Based on the assumption that mass transfer boundary layer lies within 10% of channel half height, one can

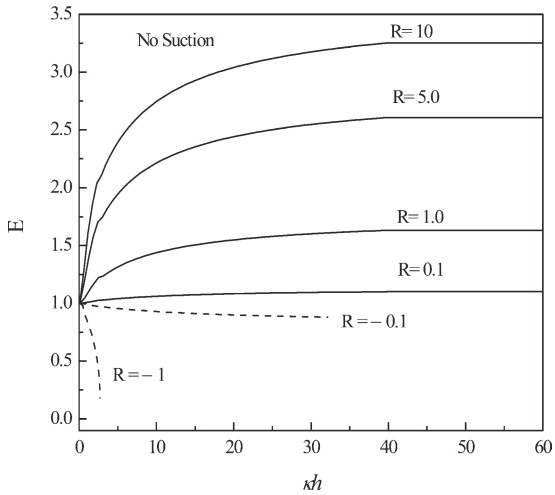

Figure 8. Variation of Sherwood number enhancement with scaled Debye length and various values of *R*. Solid lines: E_x assisting the flow; Dashed lines: E_x opposing the flow.

consider δ^* is less than 0.1 from section 2.3, it can be written as $\left(\frac{x^*}{A_1}\right)^{1/3}$ is less than 0.1. At the exit point of the microchannel, i.e., $x^* = 1$, A_1 is greater than 10^3. Hence, $\frac{3}{16}\frac{u_0 m d_e^2}{DL}$ should be greater than 10^3. Solute diffusivity varies between 10^{-10} and 10^{-11} m^2/s, making the range of Schmidt number in between 10^4 and 10^5. Therefore, the range of $\mathrm{Re}Scd_e/L$ is in between 4000 and 10,000. Since, the axial velocity is in the order of 10^{-2} m/s where as the permeation velocity in the order of 10^{-5} – 10^{-6} m/s., therefore, it can safely be assumed that the axial velocity profile (Eq. 4a) remains unaltered by the presence of the permeation of this magnitude. The parameter R varies from 0 to ∞, encompassing pure poiseulle flow to purely electroosmotic flow (electric field assisting the flow).Value of R can also be negative, in this case electric field opposes the flow.

Results and Discussion

Effect of scaled Debye length and R *on Sherwood number enhancement in case of no permeation*

In case of no permeation ($\overline{Pe}_w = 0$), the enhancement (E) in Sherwood number due to electroosmotic flow is quantified by Eqs. 34–36. The variation of E as a function of κh for various values of R is shown in Figure 8. In the figure, small values of R indicate that pressure-driven flow dominates and large R implies domination of electroosmic flow. When the axial electric field aids the pressure-driven flow inside the microchannel, Sherwood number increases as scaled Debye length increases and it becomes constant when scaled Debye length increases beyond 40. The electrokinetic effect becomes negligible as the thickness of electric double layer becomes extremely small and hence, the resistance offered by electric double layer (EDL) becomes smaller. Therefore, at higher values of κh, the Sherwood number is constant, and it is not influenced by electroosmotic flow. This phenomenon is also observed in case of heat transfer Sadeghi and Saidi.[32]

It may be noted from Figure 8 that Sherwood number increases with the value of R, in case of electric field assisting the flow. This implies that electroosmotic flow enhances Sherwood number and the enhancement can be as high as about 3.2 times at $R = 10$. For $R = 1$, the maximum enhancement of Sherwood number is about 60% more than that of pure Poiseuille flow. Enhancement of Sherwood number in case of electric field assisting the flow is due to the enhancement of convection in the direction of flow, imparting more shear to the mass transfer boundary layer leading to reduction of its thickness.

The reverse phenomenon is observed in case of electric field opposing the flow. In this case, as the electroosmotic flow opposes the pressure-driven flow, the effective velocity in the axial direction is reduced, thus reducing the shear on the mass transfer boundary layer. Consequently, the boundary layer grows in thickness and the Sherwood number decreases. The Sherwood number decreases as the scaled Debye length increases, the effect of electroosmotic flow becomes negligible (due to smaller thickness of the electric double layer) enhancement in Sherwood number becomes constant. It is interesting to note that for the values of R such that $R > 3\frac{1+0.08\kappa h}{1.08\kappa h}$, the argument within the power exponent in Eq. 35 becomes negative and the solution of E does not exist. This infeasible solution domain is also demonstrated in Figure 8 for $R = 1$ and κh greater than 3 and for $R = -0.1$ and greater κh than 30.

Effect of Debye length and other parameters on average Sherwood number

Variation of length averaged Sherwood number with the nondimensional Debye length is presented in Figure 9 for various levels of wall permeation. Both the cases of electric field assisting and opposing the flow are presented in the figure. It is observed that at the same level of permeation, in case of electric field assisting the flow, Sherwood number increases and reaches a maximum at $\kappa h = 40$ and becomes constant thereafter. With increase in scaled Debye length, the electrokinetic effects become negligible and resistance due to thickness of EDL becomes negligible and Sherwood number becomes constant. For example, with the conditions mentioned in Figure 9, at $\overline{Pe}_w = 100$ and at $R = 1$, average Sherwood number increases from 106 to about 120 up to κh =40 and it is

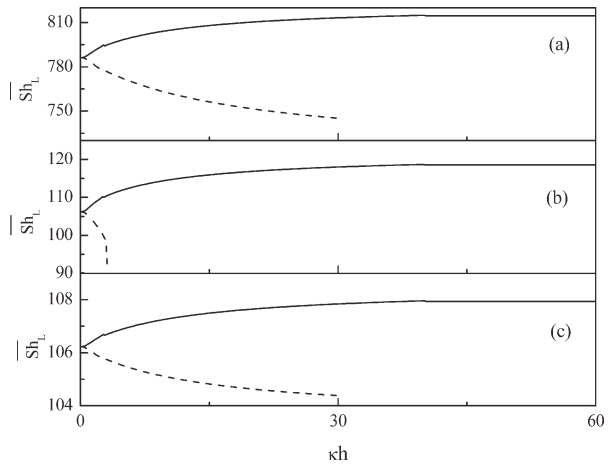

Figure 9. Variation of average Sherwood number with scaled Debye length for various extents of permeation velocity at the wall.

Solid lines: E_x assisting the flow; Dashed lines: E_x opposing the flow. (a) $\overline{Pe}_w = 1000$, $\mathrm{Re}Scd_e/L = 4000$, $R = 0.1$ and -0.1; (b) $\overline{Pe}_w = 100$, $\mathrm{Re}Scd_e/L = 4000$, $R = 1$ and -1; and (c) $\overline{Pe}_w = 100$, $\mathrm{Re}Scd_e/L = 4000$, $R = 0.1$ and -0.1.

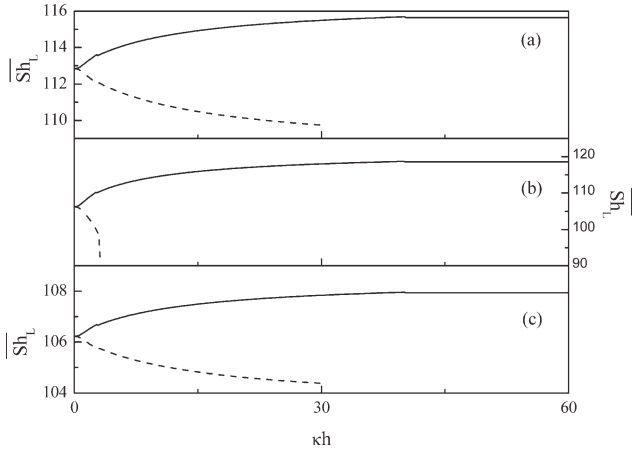

Figure 10. Variation of average Sherwood number with Debye length for various ReScd_e/L.

Solid lines: E_x assisting the flow; Dashed lines: E_x opposing the flow. (a) $\overline{Pe_w} = 100$, ReSc$_e$/L = 10000, $R = 0.1$ and -0.1; (b) $\overline{Pe_w} = 100$, ReSc$_e$/L = 4000, $R = 1$ and -1; and (c) $\overline{Pe_w} = 100$, ReScd_e/L = 4000, $R = 0.1$ and -0.1.

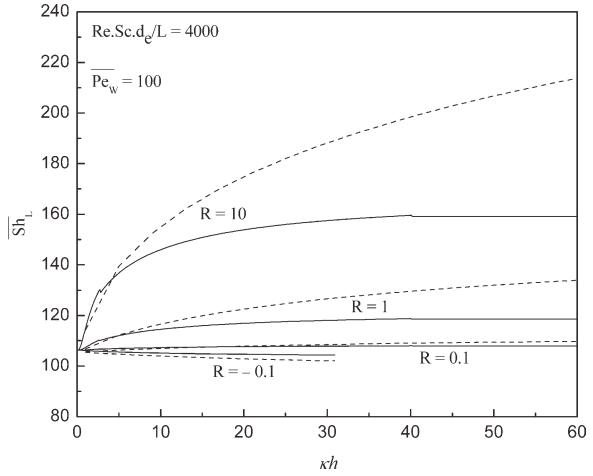

Figure 11. Comparison of average Sherwood number obtained from analytical solution and numerical solution and its variation with Debye length for various values of R.

Solid lines: analytical solution; Dashed lines: numerical solution.

constant thereafter. Thus, under these conditions, about 13% enhancement in Sherwood number is obtained. As the permeation level in the channel wall increases, the average Sherwood number increases at a fixed value of κh. As the wall permeation increases, the resistance offered by the mass transfer boundary layer decreases leading to a consequent enhancement of Sherwood number. For example, average Sherwood number increases from 108 to about 800 as the average Peclet number at the wall increases from 100 to 1000 corresponding to a scaled Debye length of 40 and thereafter.

The effects of electric field opposing the bulk flow are depicted by the dashed lines in Figure 9. The Sherwood number decreases with scaled Debye length and reaches a minimum at $\kappa h = 40$ and then it is constant as κh increases. The explanation of this behavior is already provided in context of Figure 8. The maximum reduction in Sherwood number is about 3.8% (from 780 to 750) in case of $\overline{Pe}_w = 1000$.

Variation of average Sherwood number with κh at different values of ReScd_e/L is shown in Figure 10, at constant nondimensional permeation velocity 100 and $R = 1$ and 0.1. The figure shows usual trend that Sherwood number increases with κh, reaches a maximum at $\kappa h = 40$ and becomes constant thereafter, in case of electric field assisting the flow. In case of electric field opposing the flow, the Sherwood number decreases with κh and becomes constant beyond $\kappa h = 40$. At a fixed κh, Sherwood number increases with ReScd_e/L. For same solute and channel dimensions, Sherwood number increases with Reynolds number. As Reynolds number increases, a sweeping action by the forced convection of the bulk flow is imposed on the porous wall, leading to a decrease in the solute concentration at the wall. This imparts an increase in the diffusive flux away from the wall to the bulk solution and leads to an augmentation in the mass transfer coefficient and subsequently, the Sherwood number. At $\kappa h = 40$, the average Sherwood number is about 108 at ReSc$_e$/L = 4000. This increases to about 116 when ReSc$_e$/L increases to 10,000.

Variation of average Sherwood number obtained from both analytical and numerical solution with the parameter R is shown in Figure 11. Deviation of analytical solution from numerical solution is shown in Figure 12. At low values of R and κh, deviation is less; as the values of R and κh are increasing, the deviation also increases. Figure 11 shows that Sherwood number increases with the parameter R (more electroosmotic flow), in case the electric field assisting the flow and decreases in case of electric field opposing the flow. As electroosmotic flow increases, the overall axial velocity in the channel increases, resulting in an increase in the mean flow velocity and enhanced shear accompanied with a decrease in the thickness of the mass transfer boundary layer. This leads to increase in Sherwood number. For example, at $\kappa h = 40$, Sherwood number increases from about 108 to 160, as R increases from 0.1 to 10. In case of electric field opposing the flow, the mean velocity in the channel decreases and therefore the shear on the mass transfer boundary layer becomes less, allowing the increase in thickness of the boundary layer and reduction in Sherwood number. At $\kappa h = 3$, Sherwood number decreases from about 105 to about 88 as R decreases from -0.1 to -1 , in case of electric field opposing the flow.

Figure 12 shows phase space plot for deviation of average Sherwood number obtained from analytical solution with

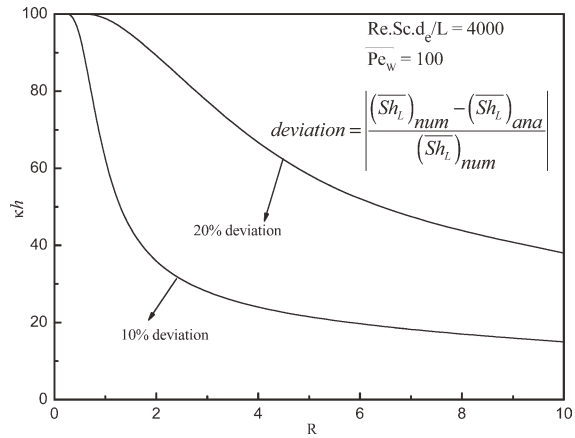

Figure 12. Phase plot of average Sherwood number deviation at different values of Debye length and R.

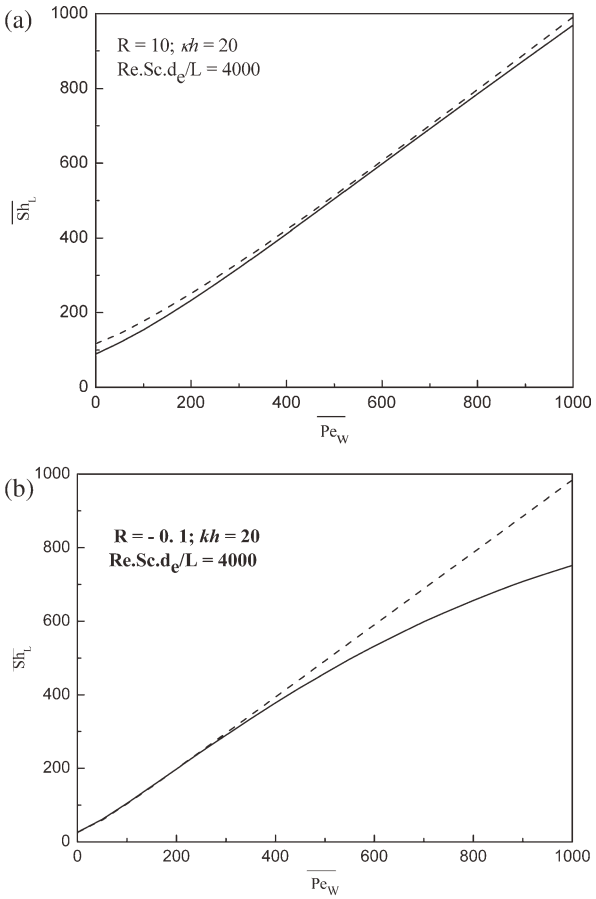

Figure 13. (a) Comparison of average Sherwood number obtained from analytical solution and numerical solution and its variation with wall permeation at κh =20 and R = 10.

Solid lines: analytical solution; Dashed lines: numerical solution. (b) Comparison of average Sherwood number obtained from analytical solution and numerical solution and its variation with wall permeation at $\kappa h = 20$ and $R = -0.1$. Solid lines: analytical solution; Dashed lines: numerical solution.

respect to that obtained from numerical solution for different values of κh and R. The concentration field (Eq. 14) with exact velocity profile (Eq. 4a) is solved numerically and the values of average Sherwood number are compared with the analytical solution. As shown in Figure 11, it is observed that for $R = -0.1$ to 0.1, the matching of numerical and analytical solution is remarkably high. For $R = 1$ and 10, the maximum deviation is 14 and 25% in the studied range of $\kappa h = 1$ to 60. It is again emphasized that there exists a combination of parameters where the maximum deviation between numerical and analytical solution is less than 10 and 20% as reported in Figure 12. It is evident that for all values of κh (up to 100) the approximate solution matches with numerical results for $R = 1$ within a deviation of maximum 10%. Up to $\kappa h = 20$, the analytical solution is within 10% of the numerical results for positive values of R less than 10.

If the deviation of 20% is considered between numerical and analytical solution the domain of parameters κh and R relaxes significantly, thereby increasing the applicability of the model.

Effect of wall permeation on average Sherwood number

Comparison of average Sherwood number obtained from both analytical and numerical solution and their variation with nondimensional permeation velocity is presented in Figures 13a,b. These figures clearly indicate that the Sherwood number increases with permeation velocity for both the cases of electric field assisting and opposing the flow. For $R = 10$ ($\kappa h = 20$), the numerical profile corroborates almost equally with the analytical solution but for $R = -0.1$ the analytical solution deviates away from the numerical solution at Pe_w above 500. However, it must be noted that the analytical solution predicts closely with the numerical solution for Pe_w less than 400 for all values of R. As discussed earlier, enhancement in wall permeation reduces the thickness of mass transfer boundary layer and thereby, increasing Sherwood number. In case of electric field opposing the flow, Sherwood number increases from about 30 to about 730 as the wall permeation velocity increases from 0 to 1000 at $\kappa h = 20$ and at $R = -0.1$.

Variation on local Sherwood number

The profiles of Sherwood number along the channel length for various levels of permeation velocity ($\overline{Pe_w}$), R, κh, and $\mathrm{ReSc}d_e/L$ are presented in Figure 14. It is observed that at a fixed axial location, Sherwood number increases with permeation velocity (Curves 1 and 2), $\mathrm{ReSc}d_e/L$ (Curves 2 and 3), and R (Curves 3 and 4). Sherwood number increases as κh increases from 1 to 10 (Curves 4 and 5). Under fixed operating conditions, Sherwood number decreases sharply at the channel entrance (within 20% of channel length) and gradually thereafter. Near the entrance, the thickness of mass transfer boundary layer is small, indicating lower values of wall concentration. Therefore, the difference between the bulk and wall concentration of the solute is quite large, resulting in higher mass transfer (by diffusion) and large values of Sherwood number. In the downstream sections of the channel, the wall concentration increases as the mass transfer boundary layer develops. This leads to a reduction in mass

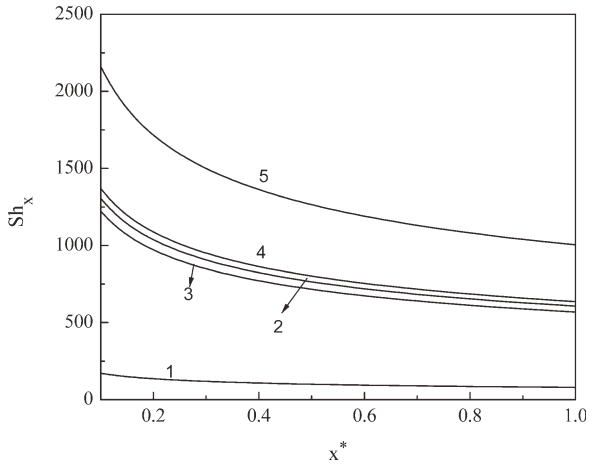

Figure 14. Variation of local Sherwood number with channel length.

Curve 1: $\overline{Pe_w} = 100$, $\mathrm{ReSc}d_e/L = 7000$, $R = 1$, and $\kappa h = 1.0$; Curve 2: $\overline{Pe_w} = 1000$, $\mathrm{ReSc}d_e/L = 7000$, $R = 1$, and $\kappa h = 1.0$; Curve 3: $\overline{Pe_w} = 1000$, $\mathrm{ReSc}d_e/L = 4000$, $R = 1$, and $\kappa h = 1.0$; Curve 4: $\overline{Pe_w} = 1000$, $\mathrm{ReSc}d_e/L = 4000$, $R = 3$, and $\kappa h = 1.0$; and Curve 5: $\overline{Pe_w} = 1000$, $\mathrm{ReSc}d_e/L = 4000$, $R = 3$, and $\kappa h = 10$.

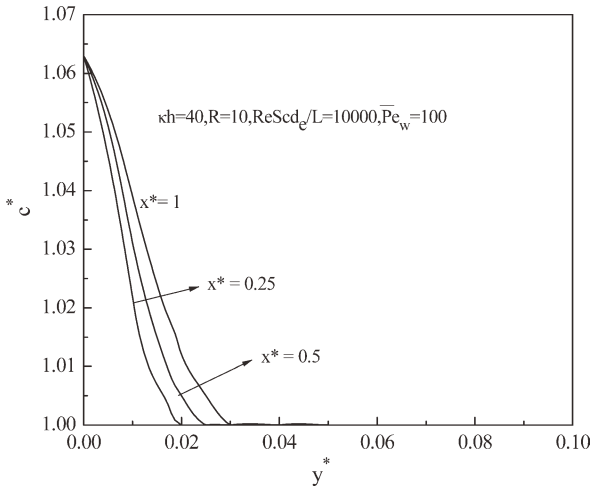

Figure 15. Concentration profiles across the cross section at various axial locations of the microchannel.

transfer as the concentration gradient at the wall decreases and subsequently, Sherwood number decreases in the downstream sections of the microchannel.

Variation on concentration profiles in the microchannel

The profiles of solute concentration along the cross section of the channel at various axial locations of the microchannel are shown in Figure 15 for values of parameters $R = 10$, $\kappa h = 40$, and $\overline{Pe}_w = 1000$. It can be observed that the solute concentration reaches the bulk concentration at about 2.0% of channel half height at $x^* = 0.25$. At the end of the channel, the mass transfer boundary layer occupies about 3.0% of the channel half height.

Concluding Remarks

Electrokinetic effects influence the mass transfer of a neutral solute in a porous microchannel. The influence is governed by whether the electroosmotic flow is aiding or opposing the pressure-driven flow. An analytical expression for the Sherwood number is developed to quantify the mass transfer. Effects of Debye length, Reynolds number, permeation velocity, etc., on Sherwood number are observed. Sherwood number enhancement is maximum at $\kappa h = 40$. At higher κh, the electrokinetic effects become negligible and Poiseuille flow becomes dominant. Permeation velocity and Reynolds number enhance the Sherwood number significantly.

In summary, transport of an electrically neutral solute can be influenced in a purely mass transfer governed manner owing to the electrokinetic effects on the electrolyte solution in a charged microchannel. This effect maximizes in the vicinity of $\kappa h = 40$. One should consider these effects in microscale transport processes involving transport of neutral solutes dissolved or suspended in an electrolyte solution in charged microchannels. Although we have imposed an external electric field in our simulations, even pressure-driven flows through such charged channels can create a counteracting electric field (streaming potential), that can adversely influence the mass transfer of the solute. The mass transfer correlation and its limiting forms can be useful design tools for microfluidic and hollow fiber filtration systems.

Acknowledgments

Financial support from Shastri Indo-Canadian Foundation is gratefully acknowledged. Support from the NSERC Industrial Research Chair in Water Quality Management for Oil Sands Extraction is gratefully acknowledged.

Notation

A_0 = dimensionless quantity defined in Eq. 13
A_1 = dimensionless quantity defined in Eq. 15 $\left(\frac{3}{16}\mathrm{Re}Sc\frac{d_e}{L}m(\kappa h,R)\right)$
B = dimensional parameter defined in Eq. 19 $\left(\frac{Pe_w x^3}{4A_1^{1/3}}\right)$
C = concentration of solute, kg/m^3
c_0 = bulk concentration of solute, kg/m^3
c_w = solute concentration at wall, kg/m^3
d_e = equivalent diameter, m
D = solute diffusivity, m^2/s
E_x = electric field strength, V/m
f = defined in Eq. 6
g = defined in Eq. 7
h = channel half height, m
I = definite integral defined in Eq. 22 $\left(\int_0^\infty \exp\left(-\frac{\eta^3}{3} - B\eta\right)d\eta\right)$
$K_{1,2}$ = integration constants
k = mass transfer coefficient, m/s
L = channel length, m
m = defined in Eq. 12
Pe_w = dimensionless permeation velocity $(v_w d_e/D)$
p = pressure, Pa
p_x = pressure gradient in axial direction, Pa/m
R = ratio defined as u_{HS}/u_p
Re = Reynolds number $(\rho u_0 d_e/\mu)$
Sc = Schmidt number $(\mu/\rho D)$
Sh = Sherwood number (kd_e/D)
u_x = axial velocity component, m/s
u_0 = cross section average velocity, m/s
u_p = average velocity for poiseuille flow, m/s
u_{HS} = Helmholtz-Smolouchoski velocity, m/s
v_y' = transverse velocity component, m/s
v_w = permeation velocity, m/s
x = axial coordinate, m
y = transverse coordinate from the wall, m

Greek letters

δ = mass transfer boundary layer thickness, m
ε = dielectric constant of medium, C/V.m
κ = inverse of Debye length, m^{-1}
μ = viscosity, Pa.s
η = similarity parameter $\left(A_1^{\frac{1}{3}}\frac{y^*}{x^{*\frac{1}{3}}}\right)$
ζ = zeta potential, V

Superscript

* = nondimensional quantities
_ = averaged quantities

Literature Cited

1. Hill RJ. Electric-field-enhanced transport in polyacrylamide hydrogel nanocomposites. *J Colloid Interface Sci*. 2007;316:635–644.
2. Kapellos GE, Alexiou TS, Payatakes AC. A multiscale theoretical model for diffusive mass transfer in cellular biological media. *Math Biosci*. 2007;210:177–237.
3. Matos MA, White LR, Tilton RD. Electroosmotically enhanced mass transfer through polyacrylamide gels. *J Colloid Interface Sci*. 2006; 300:429–436.
4. Burgreen D, Nakache FR. Electrokinetic flow in ultrafine capillary slits. *J Phys Chem*. 1964; 68:1084–1091.
5. Horiuchi K, Dutta P. Joule heating in electroosmotically driven microchannel flow. *Intl J Heat Mass Transfer*. 2004; 47:3085–3095.
6. Mala G, Li D, Dale JD. Heat transfer and fluid flow in microchannel. *Inlt J Heat Mass Transfer*. 1997; 40:3079–3088.
7. Masliyah JH, Bhattacharjee S.*Electrokinetic and Colloid Transport Phenomena*.New Jersey:Wiley, 2006.
8. Rice CL, Whitehead R. Electrokinetic flow in a narrow cylindrical capillary. *J Phys Chem*. 1965;69:4017–4024.

9. Soong CY, Wang SH. Theoretical analysis of electrokinetic flow and heat transfer in a microchannel under asymmetric boundary conditions. *J Colloid Interface Sci*. 2003;265:202–213.
10. Jacazio G, Probstein RF, Sonin AA, Young D. Electrokinetic salt rejection in hyperfiltration through porous materials: theory and experiments. *J Phys Chem*. 1972;76:4015–4023.
11. Bhattacharjee S, Chen JC, Elimelech M. Coupled model of concentration polarization and pore transport in crossflow nanofiltration. *AIChE J*. 2001; 47:2733–2745.
12. De S, Bhattacharjee S. Flux decline during cross flow membrane filtration of electrolytic solution in presence of charged nano-colloids: a simple electrokinetic model. *J Colloid Interface Sci*. 2011; 353:530–536.
13. Liu C, Sun Y, Siddiqui O, Chien YW, Shi WM, Li J. Blood glucose control in diabetric rats by transdermal iontophoretic delivery of insulin. *Intl J Pharm*. 1988; 44:197–204.
14. Zhang I, Shung KK, Edwards DA. Hydrogels with enhanced mass transfer for transdermal drug delivery. *J Pharm Sci*. 1996; 85:1312–1316.
15. Nazemifard N, Bhattacharjee S, Masliyah JH, Harrison DJ. DNA dynamics in nanoscale scale confinement under asymmetric pulsed field electrophoresis. *Angew Chem Int Ed Engl*. 2010; 49:3326–3329.
16. Molla SH, Bhattacharjee S. Dielectrophoretic levitation in the presence of shear flow: implications for colloidal fouling of filtration membranes. *Langmuir*. 2007; 23:10618–10627.
17. Molla SH, Bhattacharjee S. Tunable filtration media employing alternating current electrokinetics. *Langmuir*. 2008; 24:5659–5662.
18. Molla SH, Bhattacharjee S. Prevention of colloidal membrane fouling employing dielectrophoretic forces on a parallel electrode array. *J Membr Sci*. 2005; 255:187–199.
19. Molla SH, Masliyah JH, Bhattacharjee S. Simulation of dielectrophoretic membrane filtration process for removal of water droplets from water-in-oil emulsions. *J Colloid Inetrface Sci*. 2005; 287:338–350.
20. Kang Y, Yang C, Huang X. AC electroosmosis in microchannels packed with a porous medium. *J Micromech Microeng*. 2004; 14: 1249–1257.
21. Banga AK, Chien YW. Iontophoretic delivery of drugs: fundamentals, developments, and biomedical applications. *J Controlled Release*. 1998; 7:1–24.
22. Siddiqui O, Sun Y, Liu JC, Chien YW. Facilitated transdermal transport of insulin. *J Pharm Sci*. 1987; 76:341–345.
23. Brown MC, Trayanor MJ, Martin GP,*Rankin, Transdermal drug delivery systems*, In:Jain KK, editor.*Drug Delivery Systems*.NJ:Humana,119–124.
24. Gramer MJ, Poeschl DM, Comparison of cell growth in T-flasks, in micro hollow fiber bioreactors, and in an industrial scale hollow fiber bioreactor system, *Cytotechnology* 34:111–119, 2000.
25. Chang M, Homsy GM. Effects of Joule heating on the stability of time-modulated electro- osmotic flow. *Phys Fluids*. 2005;17: 074107–074117.
26. Hsu J, Ting O, Lee D, Tseng S, Chen C, Su A. Residence time distribution for electrokinetic flow through a microchannel comprising a bundle of cylinders. *J Colloid Interface Sci*. 2007; 307:265–271.
27. Kamish F, Oztop HF. Second law analysis of 2D laminar flow of two immiscible incompressible viscous fluids in a channel. *Heat Mass Transfer*. 2008; 44:751–761.
28. Wang C, Wong TN, Yang C, Ooi KT. Characterisation of electroosmotic flow in rectangular microchannels. *Intl J Heat Mass Transfer*. 2007; 50:3115–3121.
29. Yan DG, Yang C, Huang XY. Effect of finite reservoir size on electroosmotic flow in microchannels. *Microfluid Nanofluid*. 2007;3:333–340.
30. Zhaou T, Liu A, He F, Xia X. Time dependent starting profile of velocity upon application of external electric potential in electroosmotic driven microchannel. *Colloids Surf: A physic- Chem Eng Asp*. 2007; 277:136–144.
31. Zade AQ, Manzani MT, Hannani SK. An analytical solution for thermally fully developed combined pressure-electroosmotically driven flow in microchannel, *Intl J Heat Mass Transfer*. 2007; 50:1087–1096.
32. Sadeghi A, Saidi MH. Viscous dissipation effects on thermal transport characteristics of combined pressure and electroosmotically driven flow in microchannels. *Int J Heat Mass Transfer*. 2010; 53:3782–3791.
33. Das S, Chakroborty S. Analytical solutions for velocity, temperature and concentration distribution in electroosmotic microchannel flow of a non-newtonian biofluid. *Anal Chem Acta*. 2006; 559:15–24.
34. Liapis AI, Grimes BA. Film Mass Transfer coefficient expressions for electroosmotic flows. *J Colloid Interface Sci*. 2000; 229:540–543.
35. McCabe WL, Smith JC, Harriot P.*Unit Operations of Chemical Engineering*.Singapore:McGraw-Hill, 1993.

Manuscript received Mar. 1, 2011, and revision received May 14, 2011.